International Journal of Heat and Fluid Flow 29 (2008) 1567–1576

Contents lists available at ScienceDirect

International Journal of Heat and Fluid Flow

journal homepage: www.elsevier.com/locate/ijhff

Flow structure in the locked-on wake of a circular cylinder in pulsating flow: Effect of forcing amplitude

E. Konstantinidis [a,*], S. Balabani [b]

[a] Department of Engineering and Management of Energy Resources, University of Western Macedonia, Bakola and Sialvera, Kozani 50100, Greece
[b] Department of Mechanical Engineering, King's College London, Strand WC2R 2LS, United Kingdom

ARTICLE INFO

Article history:
Received 21 April 2008
Received in revised form 16 July 2008
Accepted 14 August 2008
Available online 7 October 2008

Keywords:
Pulsating flow
Forced wake
PIV

ABSTRACT

The wake structure of a circular cylinder in non-reversing pulsating flow is investigated by means of particle image velocimetry. Measurements are reported for pulsations at twice the natural frequency of vortex shedding in the unforced wake and for forcing amplitudes up to 23% at a constant Reynolds number of 2150. For the parameters employed the vortex shedding locks-on to the sub-harmonic of the pulsation frequency and a resonant wake is formed. The mean velocity field and the distributions of the total and coherent Reynolds stresses show that the averaged wake structure is systematically modified by the flow pulsations. It is shown that this modification is caused by changes in the dynamics of vortex formation and shedding primarily in the near wake. The recirculation bubble and the vortex formation region decrease in size, the global peak values in the distributions of the total and coherent Reynolds stresses increase asymptotically whereas the vortex strength and the mean drag coefficient increase almost linearly with increasing forcing amplitude. The measures of the minimum wake width in the formation region do not exhibit any variation with amplitude even though the wake downstream of the formation region is wider in pulsating flow due to the increased strength of the shed vortices.

1. Introduction

The control of the wake structure behind a circular cylinder can be considered as a paradigm for control of unsteady separated flows. Both active and passive methods have been reported in the published literature to achieve multifaceted objectives such as drag reduction, heat/mass transfer intensification, mixing enhancement, and noise/vibration suppression. Pertinent reviews on the subject can be found in Griffin and Hall (1991) and most recently in Choi et al. (2008) among others. Passive control is achieved primarily by modification of the cylinder geometry, e.g., by the addition of helical strakes, bumps or tabs on the external surface which induce a three-dimensional perturbation in the flow. In open-loop active control, the intrinsically unsteady wake is commonly perturbed by a periodic excitation such as rectilinear or rotational cylinder oscillations, flow pulsations, sound forcing, suction/blowing, synthetic jets or even surface deformations. These methods attempt to modify the dynamics of flow separation and vortex formation in nominally two-dimensional wakes. Closed-loop or feedback control schemes have also been developed but, as Choi et al. (2008) point out, such schemes require a great deal of effort and instrumentation and are thus unlikely to be implemented in practical situations. Therefore, the investigation of open-loop and feedback control methods should continue in parallel in order to achieve the desired objectives.

The present study examines the wake structure of a circular cylinder in pulsating flow, i.e. an unsteady non-reversing flow with forced sinusoidal fluctuations superimposed on the average flow velocity. Pulsating flow offers a potential method of controlling the wake structure via the frequency and amplitude of forcing and is relevant to many engineering applications. Most of the previous work on this subject has concentrated on vortex shedding lock-on, i.e. the regime in which the vortex shedding frequency is controlled by the pulsation frequency. Barnes and Grant (1983) were possibly the first to show that there is a range of excitation frequencies around twice the natural vortex shedding frequency for which the wake locks-on to half the pulsation frequency. A number of subsequent experimental studies have confirmed the existence of lock-on phenomenon and investigated its effects on unsteady pressure and forces (Barbi et al., 1986), the wake and turbulence structure (Armstrong et al., 1987; Konstantinidis et al., 2003; Jarza and Podolski, 2004), and heat/mass transfer (Telionis et al., 1992; Perwaiz and Base, 1992; Sung et al., 1994; Kikuchi et al., 2000). The effect of cylinder geometry on the lock-on range was also investigated from the point of view of vortex flow-meter performance (Armstrong et al., 1986; Al-Asmi and Castro, 1992; Wolochuk et al., 1996). More recently, particle image velocimetry (PIV) has been employed to characterize in detail the wake structure in pulsating flow under lock-on conditions (Kim et al., 2006;

* Corresponding author. Tel.: +30 24610 56754.
E-mail address: ekonstantinidis@uowm.gr (E. Konstantinidis).

0142-727X/$ - see front matter © 2008 Elsevier Inc. All rights reserved.
doi:10.1016/j.ijheatfluidflow.2008.08.002

Konstantinidis et al., 2005a) and the modification in the vortex shedding patterns (Konstantinidis et al., 2005b, 2007). Despite the large number of studies cited above, the effect of pulsation amplitude on the wake structure has not been considered systematically due to associated experimental difficulties in producing good quality pulsations of various amplitudes in flow facilities. Using a purpose-built facility for pulsating flow, it was made possible to overcome the above limitations. In a previous study, the effect of pulsation amplitude on the flow characteristics along the wake centerline was considered briefly through point-wise measurements using laser Doppler velocimetry (Konstantinidis et al., 2003). The present paper is an extension of that work to planar measurements using PIV in order to gain a better understanding of the effect of pulsation amplitude.

In addition to the above-stated objective, the flow about a circular cylinder has been widely accepted as a test case for the validation of numerical codes in computational fluid dynamics, (see, e.g., Breuer, 2000). However, the emphasis has been placed on the relatively simple case of a cylinder in uniform steady flow. With the increasing application of flow control it becomes increasingly important to verify that the numerical schemes can predict accurately the changes brought about to the flow field by active and passive control methods such as perturbations of the flow or the geometry. The present study provides information on the mean velocity field, the distribution of the total and coherent Reynolds stresses in the locked-on wake of a circular cylinder, and on global wake parameters that may be readily used for verification purposes, i.e. the recirculation bubble and vortex formation lengths, maximum Reynolds stresses and vortex strength as well as the drag force coefficient and their variations as a function of the forcing amplitude.

2. Experimental techniques

The experiments were conducted in a recirculating-type water rig purpose-built to generate pulsating flow. Its main feature is the independent control of the frequency and the amplitude of the imposed flow pulsations produced by periodically blocking part of the flow via a rotating slot valve. By adjusting the ratio of perturbed/unperturbed flow different pulsation amplitudes can be achieved. The pulsating inflow velocity can be approximated as a sinusoidal function of time

$$U(t) = U_m + \frac{\Delta U}{2}\sin(2\pi f_e t), \quad (1)$$

where U_m is the mean inflow velocity and ΔU is the peak-to-peak amplitude of velocity fluctuation and f_e is the pulsation (excitation) frequency of the flow. The inflow velocity, pulsation frequency and amplitude were monitored by a laser-Doppler system providing time-resolved velocity measurements upstream of the test model. Details of the experimental configuration have been described in previous work and will not be repeated here in full (see Konstantinidis et al., 2003, 2005a, 2007). Briefly, the flow passes through a honeycomb, a series of perforated plates and a 9:1 area-ratio contraction and enters the test section having a uniform profile with a variation less than 1% in the core and a turbulence intensity of 3%. The cross-sectional area of the test section measures $72 \times 72\ mm^2$. An acrylic circular rod with polished surface, 7.2 mm in diameter, was mounted horizontally in the centre of the test section. This configuration results in an aspect ratio of length/diameter of 10 and a flow blockage of 10%. It is well known from previous studies that the aspect ratio and blockage introduce three-dimensional effects and distort the flow around the cylinder compared to the canonical case of unconfined flow around infinitely long cylinders in a complex way. Although it is expected that these parameters do not have a considerable effect, strictly speaking the results obtained in the present study are applicable for the particular experimental configuration employed; the cylinder aspect ratio, the flow blockage, the turbulence level of the inflow and the proximity of the test section walls are expected to have some influence. Nevertheless, the canonical case cannot be easily realized in a physical experiment; this would necessitate the use of a very small cylinder. On the other hand, there exist competing requirements for accuracy and sufficient spatial resolution of the wake field as measured by PIV. After considerable analysis of the competing requirements, a set of flow parameters which is acceptable in terms of aspect ratio and blockage was employed while at the same time PIV settings were optimized as detailed below. It is worth noting that with current computational capabilities a 3-D mesh of the entire flow configuration can be constructed so that numerical predictions may be directly compared against the present experiments without the need to invoke *ad hoc* boundary conditions (see, e.g., Mittal, 2001).

The origin of the coordinate system was taken at the centre of the cylinder with the x-axis measured in the direction of the flow and the y-axis perpendicular to the flow and the cylinder axis. The velocity components in the x- and y-axis are denoted u and v, respectively.

The instantaneous velocity fields in the wake behind the cylinder model were measured with a double-pulsed particle image velocimeter (PIV). The system consists of a continuous Ar–Ion laser source, a high-resolution PCO SensiCam digital camera (1024×1240 pixels^2), an electro-optical shutter connected to a synchronization unit for producing light pulses and setting the pulse delay and an acquisition board on a personal computer as shown schematically in Fig. 1. The fluid was seeded with 10 μm silver-coated hollow-glass spheres with a specific gravity of 1.1 and the wake was illuminated by a 800-μm thick laser sheet perpendicular to the cylinder axis at midspan. The field of camera view, i.e. the measurement domain is $0.35 < x/d < 7.5$ and $-3 < y/d < 3$. Image pairs were analyzed by employing an adaptive cross-correlation methodology on 32×32 pixels^2 interrogation windows with 50% overlap (Konstantinidis et al., 2005a). For these PIV settings, the optimization criteria regarding the particle image density, the relative in-plane motion, the relative out-of-plane motion and the velocity gradient parameter suggested by Keane and Adrian (1990) were satisfied. This method of analysis yields 4584 velocity vectors in each instantaneous field excluding the regions covered by the cylinder and its shadow. The spatial resolution of the measurement grid is approximately 0.1 d which is sufficient to resolve the flow scales of interest in the present study. Due to the slow response time of the image acquisition system, the sampling fre-

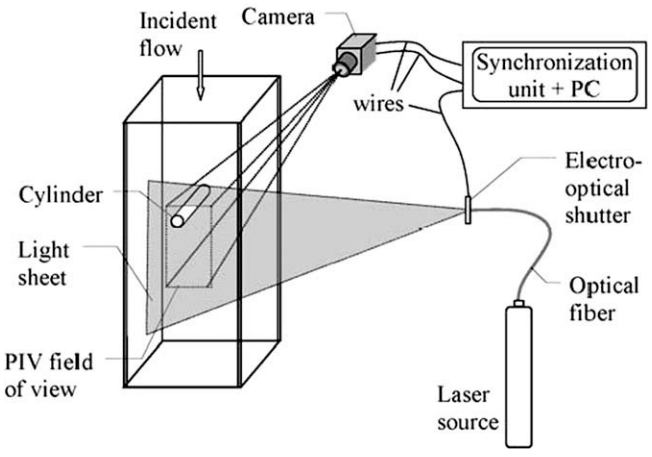

Fig. 1. Schematic of the experimental set-up.

quency (1 Hz) was much lower than that of the pulsations or that of vortex shedding. Therefore, the instantaneous velocity fields are statistically independent. A total number of 450–480 snapshots of the velocity field were obtained for further statistical processing.

3. Results and analysis

The results reported in this paper were obtained for steady (unforced) and pulsating (forced) flow at a Reynolds number of $Re = 2150$ based on the cylinder diameter, the inflow mean velocity and the kinematic viscosity of water. The pulsation frequency was maintained constant at $f_e = 17.8$ Hz which is twice the natural vortex shedding frequency in the unforced wake, f_{v0}. The corresponding Strouhal number in steady flow is equal to $St = 0.215$. The pulsation amplitude was varied resulting in velocity amplitude ratios of $\Delta U/U_m = 0.08$, 0.12, 0.18 and 0.23 peak-to-peak. The above parameters in the frequency–amplitude space correspond to the vortex shedding lock-on regime well above the threshold limit (see Konstantinidis et al., 2003). In the following sections, the effect of varying the pulsation amplitude on the wake structure is examined in detail.

3.1. Mean velocity field

Fig. 2 shows the velocity vectors, contours of the velocity magnitude and streamlines of the mean flow field for three different amplitudes of imposed flow pulsation. In Fig. 2 (left column) the velocity vectors are shown at the measurement locations of the raw data as well as for data reflected in the wake axis. The raw and reflected data overlap indicating that the flow is symmetric. Further checks of the mean velocity profiles (not shown here for economy of space) verified the flow symmetry, therefore, this property was employed in order to effectively double the number of instantaneous velocity fields used for the production of the distributions of the mean velocity magnitude, streamlines and Reynolds stresses shown in Fig. 2 and subsequent figures. For steady flow without superimposed pulsations, two recirculating eddies exist in the near wake that extend to 2.1 diameters beyond the cylinder centre delineating a region of reversed flow, the so-called 'recirculation bubble'. The length of the recirculation bubble (l_b) is marked by the location along the wake axis at which the axial mean velocity is zero. The variation of the normalized recirculation bubble length with the pulsation amplitude is listed in Table 1. With increasing the amplitude, the recirculation bubble gradually shrinks in size and is nearly eliminated at the highest amplitude employed. The gradual modification of the wake structure with pulsation amplitude can also be observed in the distribution of the velocity magnitude (Fig. 2, middle column); the region of low velocities near the base of the cylinder reduces in size and the velocity defect along the wake centreline recovers more rapidly with increasing amplitude. The area of the contour of maximum velocity magnitude ($1.3U_m$) decreases in size as the pulsation amplitude increases indicating a more localized acceleration of the flow over the apex of the cylinder. The effect of amplitude is

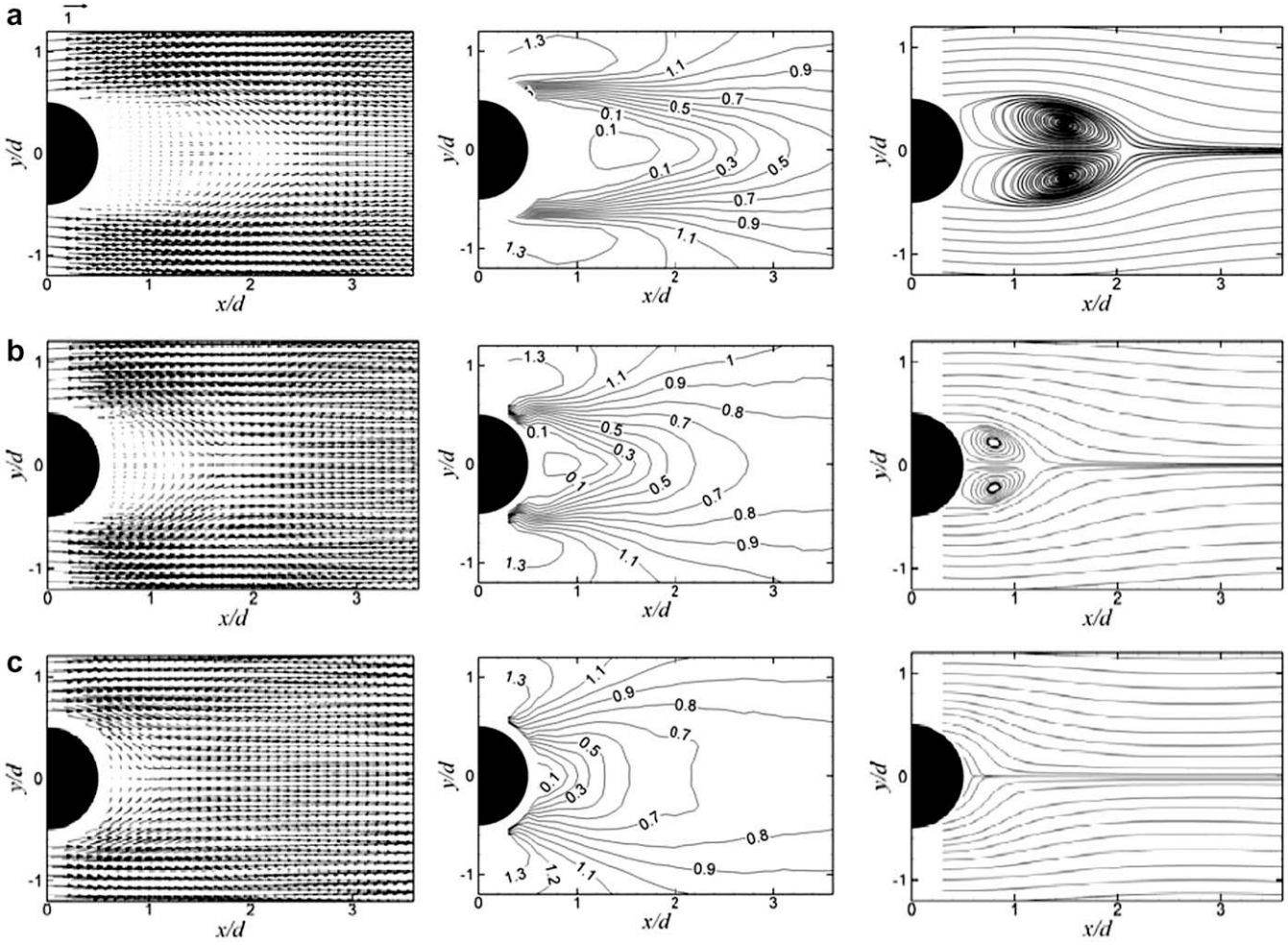

Fig. 2. Velocity vectors, contours of velocity magnitude and sectional streamlines of the mean flow field; (a) $\Delta U/U_m = 0.00$, (b) 0.08, (c) 0.23.

Table 1
Wake structure of the mean flow at different pulsation amplitudes

$\Delta U/U_m$	l_b/d	$(x/d)_{min}$	$(d_w/d)_{min}$	$(d_w/d)_{@x=5d}$
0.00	2.08	2.0	0.48	1.58
0.08	1.17	1.1	0.46	1.92
0.12	0.93	0.9	0.46	2.16
0.18	0.77	0.8	0.46	2.10
0.23	0.61	0.7	0.45	2.04

more clearly seen in the mean flow streamlines (Fig. 2, right column). It should be noted that the accuracy of the streamlines close to the cylinder surface at a distance <0.05 d is limited since no measurements were made in this region (cf. to velocity vectors). Zero velocities were assumed on the cylinder wall in order to interpolate the results in the region close to the cylinder.

One of the parameters describing the wake structure of the mean flow is the 'half-wake' width d_w which denotes the transverse distance off the wake axis marked by the mean velocity

$$\overline{U}(x, y = d_w) = \frac{\overline{U}_{max}(x) - \overline{U}_{min}(x)}{2} \tag{2}$$

where the overbar denotes time averaging. The half-width varies along the wake axis reaching a minimum value within the recirculation bubble and increasing asymptotically further downstream. Table 1 lists the location and value of the minimum half-wake width as well as its value at $x/d = 5$. The location $(x/d)_{min}$ at which the minimum half-wake width occurs follows a similar trend to that of l_b/d whereas the value of $(d_w/d)_{min}$ does not vary appreciably with the forcing amplitude. However, the half-wake width at $x/d = 5$ is approximately 30% narrower in steady flow than in pulsating flow. Note that the slight variation of d_w with forcing amplitude in pulsating flow is within the level of accuracy in determining this length scale (±0.025 d).

3.2. Total Reynolds stresses

The distribution of the total Reynolds stresses in the wake for different pulsation amplitudes is shown in Fig. 3. The conventional Reynolds decomposition is employed to segregate the instantaneous velocity field into mean and fluctuating parts

$$\begin{aligned} u_i(x, y) &= \overline{U}(x, y) + u_i'(x, y) \\ v_i(x, y) &= \overline{V}(x, y) + v_i'(x, y) \end{aligned} \tag{3}$$

Thus, the stresses shown here include contributions from both the periodic (coherent) flow fluctuations due to vortex shedding and random (incoherent) fluctuations due to turbulence. The Reynolds stresses are normalized with U_m^2. The longitudinal Reynolds stress $\overline{u'u'}$ (left column of Fig. 3) exhibits the characteristic distribution of wake flows having high intensity along the separating shear layer and two global extremes off the wake axis. With increasing amplitude, the location of the extremes moves closer to the cylinder and the corresponding values increase in magnitude. However, the transverse distance of the extremes does not change with amplitude. This accords with the concept of a universal Strouhal number St' suggested by Griffin (1978)

$$St' = \frac{f_v d'}{U_s} \tag{4}$$

where f_v is the vortex shedding frequency of the forced wake, d' is the transverse distance between extremes off the wake axis and U_s is the velocity just outside of the separating shear layer. Since f_v remains constant for the different amplitudes employed due to lock-on ($f_v = f_e/2$) and U_s is not significantly affected by the pulsations (as indicated by the distributions of the velocity magnitude in Fig. 2), it follows that d' should also remain constant. It is worth noting that the superimposition of a small-amplitude periodic pulsation in the flow results in an increase in the longitudinal total Reynolds stress. Nevertheless, the substantial increase in the magnitude of $\overline{u'u'}$ seen in Fig. 3 is far greater than that introduced by the imposed fluctuations; it results from a strong resonance between the forcing and the wake. Lower or higher excitation frequencies than $f_e/f_{v0} = 2$ employed here were found to result in a less marked increase in the longitudinal Reynolds stress. The transverse component of the Reynolds stress $\overline{v'v'}$ exhibits a single peak in the wake centreline as seen in the middle column of Fig. 3. The location of the peak moves closer to the cylinder and the peak value increases considerably with increasing the pulsation amplitude. The most striking feature of these distributions is the existence of a very strong entrainment of fluid across the wake axis, e.g., for $\Delta U/U_m = 0.23$ the magnitude of the maximum transverse velocity component corresponds to $V_{max} \approx 1.3U_m$, i.e. it far exceeds that of the mean inflow velocity and is approximately the same as the highest velocity magnitude over the apex of the cylinder. The Reynolds shear stress $\overline{u'v'}$ distribution is shown on the right column in Fig. 3. For steady flow, $\overline{u'v'}$ exhibits a distribution having two local extremes of opposite sign within the recirculation bubble followed by another two global extremes with inversed sign further downstream. As the recirculation bubble shrinks in size with increasing pulsation amplitude, the two local extremes gradually disappear and the two global extremes move closer to the cylinder in a similar way as in the distribution of the longitudinal stress. Similarly, the transverse distance between the global extremes off the wake centreline is not affected by the imposed pulsations.

3.3. Coherent Reynolds stresses

The contribution of coherent flow structures associated with periodic vortex shedding plays an important role in cylinder wakes. In order to extract the velocity fluctuations due to vortex shedding, proper orthogonal decomposition (POD) is employed. For details in the implementation of POD with PIV data the reader is referred to the works by Patte-Rouland et al. (2001) and Graftieaux et al. (2001) among others. The choice of the number of modes is a critical issue in extracting the coherent flow structures from the lot. Ma et al. (2003) found that only two POD modes are capable of reproducing the low-dimensional dynamics in unforced cylinder wakes at $Re = 610$. However, our previous study of forced cylinder wakes at $Re = 2150$ showed that six POD modes are needed to capture bimodal vortex dynamics. Furthermore, the POD modes up to the sixth order derived from the present data exhibit a sufficient degree of symmetry or anti-symmetry to indicate a repetitive modal behaviour whereas higher order modes were rather random. Therefore, it is deemed appropriate to employ six POD modes to decompose the instantaneous velocity fields into three components as

$$\begin{aligned} u_i(x, y) &= \overline{U}(x, y) + \tilde{u}_i(x, y) + u_i''(x, y) \\ v_i(x, y) &= \overline{V}(x, y) + \tilde{v}_i(x, y) + v_i''(x, y) \end{aligned} \tag{5}$$

where the tilde denotes coherent fluctuations and the double prime denotes incoherent fluctuations. The coherent fluctuations are expressed as a linear combination of the dominant POD modes

$$\begin{aligned} \tilde{u}_i(x, y) &= \sum_{j=1}^{6} \phi_u(x, y) a_{i,j} \\ \tilde{v}_i(x, y) &= \sum_{j=1}^{6} \phi_v(x, y) a_{i,j} \end{aligned} \tag{6}$$

where $\phi_u(x,y)$ and $\phi_v(x,y)$ are the empirical orthonormal POD basis functions and $a_{i,j}$ are the coefficients derived by projecting the raw velocity fields onto the POD basis.

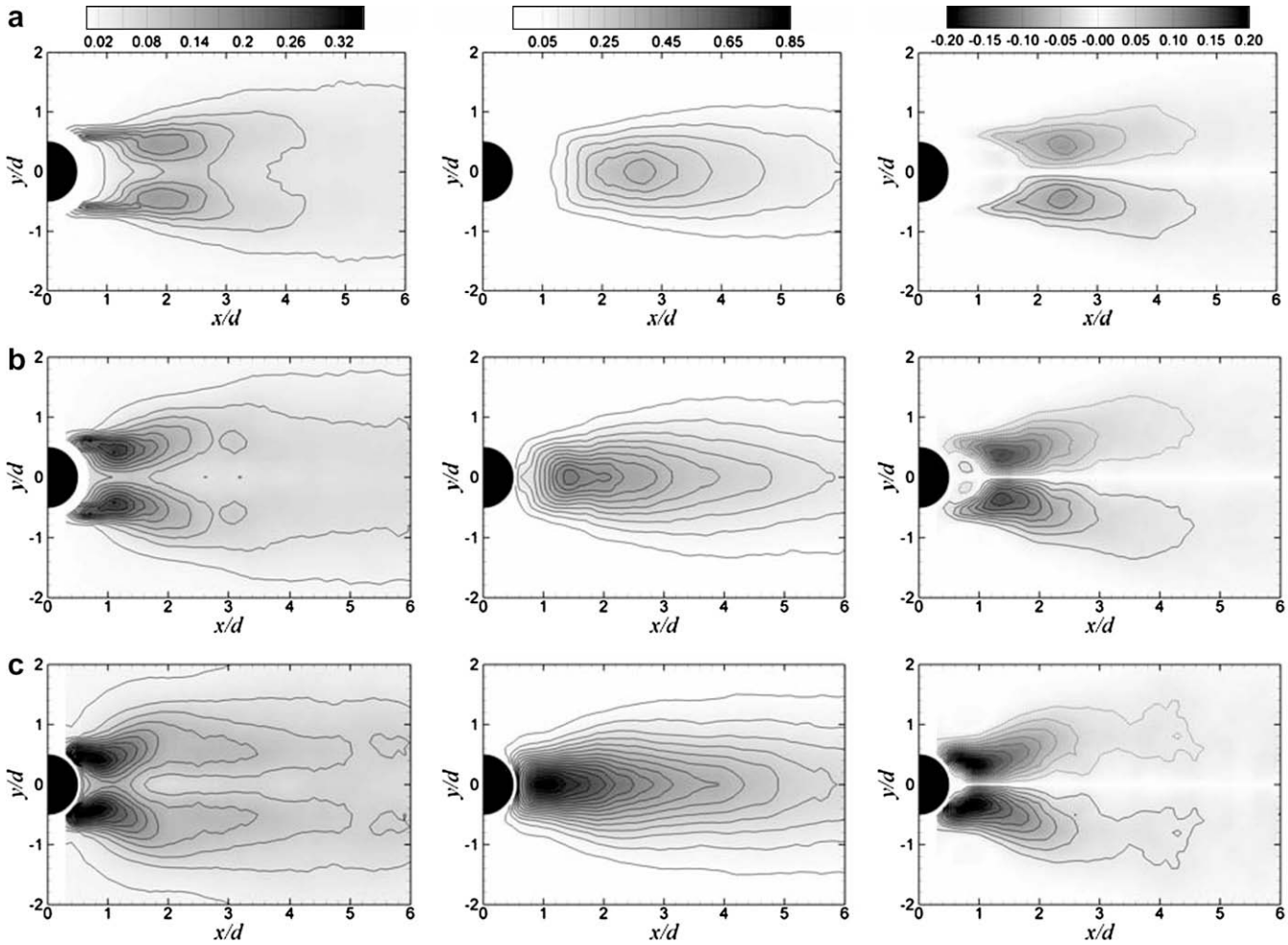

Fig. 3. Distribution of the total Reynolds stresses in the wake; left column: $\overline{u'u'}/U_m^2$, middle column: $\overline{v'v'}/U_m^2$, right column: $\overline{u'v'}/U_m^2$; (a) $\Delta U/U_m = 0.00$, (b) 0.08, (c) 0.23.

Fig. 4 shows the distribution of the coherent Reynolds stresses in the wake for different forcing amplitudes. All three coherent Reynolds stress components exhibit similar distributions to those of the corresponding total Reynolds stresses in Fig. 3 and the same trend with respect to their variation with forcing amplitude. Furthermore, the global peak values for the coherent part of the Reynolds stresses occur at approximately the same locations as those for the total part but their absolute values are slightly lower for the former as would be expected. The above observations indicate that the effect of forcing amplitude on the unsteady wake structure is predominantly associated with changes in the dynamics of vortex formation and shedding. This finding implies that turbulence effects might be of secondary importance in the overall wake dynamics; in other words, the primary effects accompanying vortex shedding lock-on might be expected to carry across a wide range of Reynolds numbers. Indeed, comparisons discussed further below support this hypothesis.

3.4. Global wake parameters

The variation of the global wake characteristics with forcing amplitude, i.e. the peak values of the Reynolds stresses and the downstream locations at which these occur, is summarized in Figs. 5 and 6. As shown in Fig. 5, the peak values for the total Reynolds stresses increase with increasing amplitude for all components but the increase is most marked for the transverse stress which is of considerably higher magnitude than the longitudinal and the shear stresses. The increase is steeper for low forcing amplitudes and gradually appears to level off as the amplitude is increased further. For both the natural and forced wake, the contribution of the coherent fluctuations to the peak Reynolds stresses is 78%, 87% and 88% on average for the longitudinal, transverse and shear components, respectively. It should be noted that preliminary tests using a different number of POD modes for steady flow indicated a minor effect on the results. However, the contribution of the coherent fluctuations appears to be higher in pulsating flow. This might be attributed to two factors: firstly, lock-on synchronizes the wakes fluctuations and the effect of cycle-to-cycle variations in the vortex formation and shedding process are alleviated. Secondly, the flow pulsations impose themselves a coherent fluctuation. As it is shown in the following section, the increase in the Reynolds stresses is partially associated with an increase in the strength of the vortices shed from the cylinder. It might be argued that the vortex strength cannot increase indefinitely with forcing amplitude and therefore it is reasonable to expect a plateau at high amplitudes. The location at which the peaks in the longitudinal and transverse total Reynolds stresses occur, denoted l_u and l_v respectively, are shown in Fig. 6. The variation of the vortex formation length l_f is also shown in the same figure. The vortex formation length was determined from the location in the wake centreline at which the fluctuations of the longitudinal velocity are maximum, a widely employed definition proposed by Griffin (1995). The length scales are normalised with the cylinder diameter in Fig. 6. The same trend is observed for all measures of the vortex

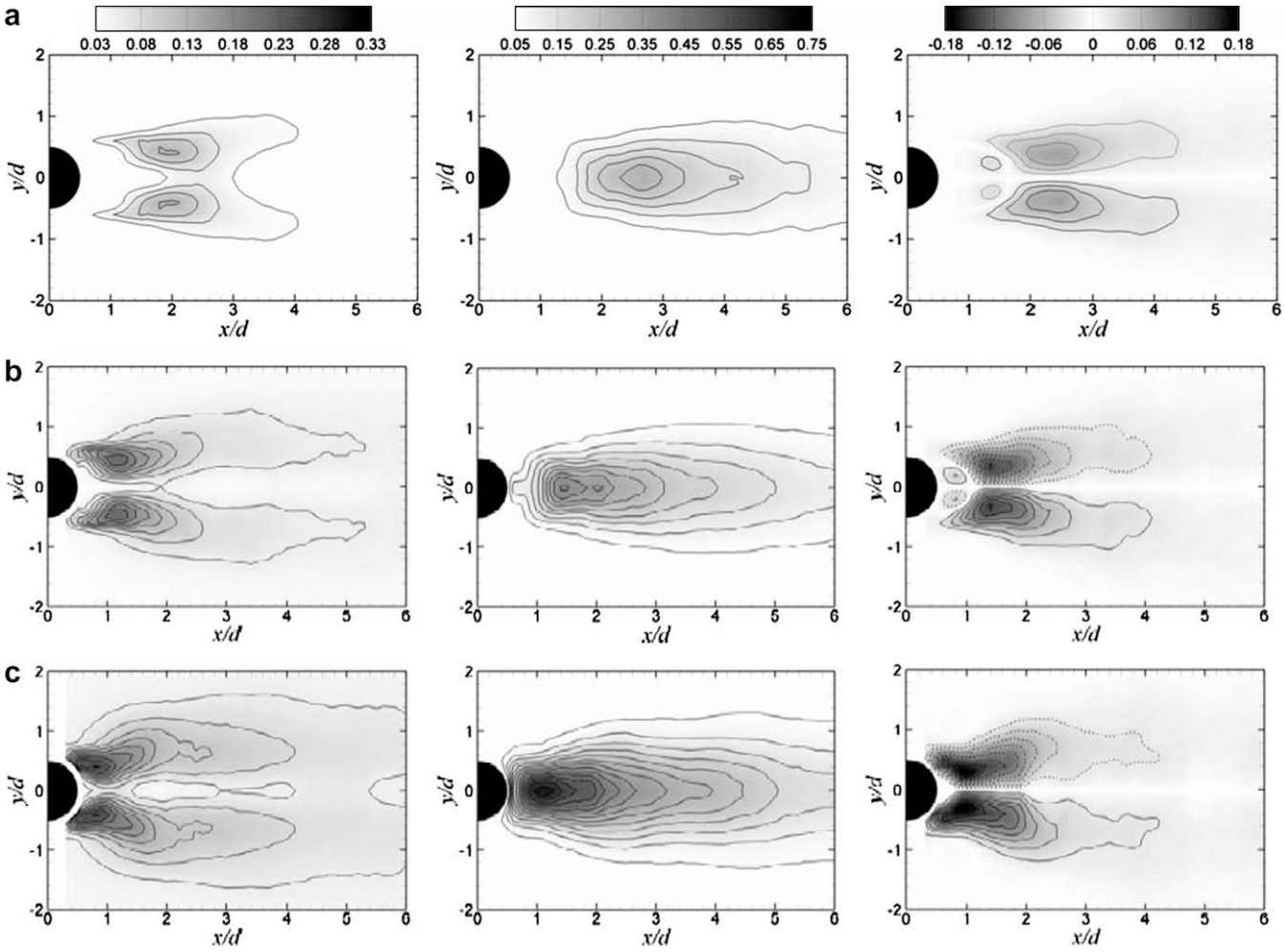

Fig. 4. Distribution of the coherent Reynolds stresses in the wake; left column: $\overline{u'u'}/U_m^2$, middle column: $\overline{v'v'}/U_m^2$, right column: $\overline{u'v'}/U_m^2$; (a) $\Delta U/U_m = 0.00$, (b) 0.08, (c) 0.23.

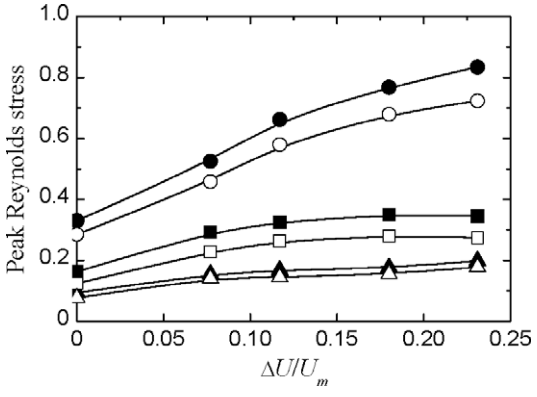

Fig. 5. Variation of the total (full symbols) and coherent (open symbols) peak Reynolds stresses with amplitude ratio; squares: $\overline{u'u'}/U_m^2$, $\overline{\tilde{u}\tilde{u}}/U_m^2$; circles: $\overline{v'v'}/U_m^2$, $\overline{\tilde{v}\tilde{v}}/U_m^2$; triangles: $\overline{u'v'}/U_m^2$, $\overline{\tilde{u}\tilde{v}}/U_m^2$.

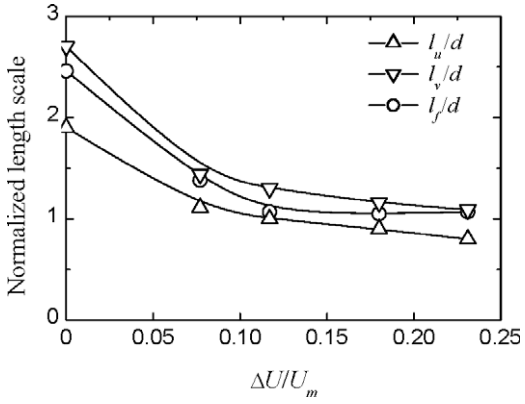

Fig. 6. Variation of the locations of maximum longitudinal and transverse velocity fluctuations in the wake centreline and of the vortex formation length with amplitude ratio.

formation region with forcing amplitude, i.e. a gradual decrease with increasing forcing amplitude up to a limit imposed by the presence of the cylinder.

Table 2 provides a comparison of the global peak Reynolds stresses shown in Fig. 5 with other published data for both steady and pulsating flow (Kim et al., 2006). The present data reported in the table for pulsating flow refer to the same forcing amplitude (10% peak-to-peak) employed by Kim et al. and were obtained by linear interpolation among the measured data. It can be observed that for steady flow, the peak values for the longitudinal and transverse total stress components in the natural wake are approximately 12% lower in the present study compared to those by Kim et al. for a lower Reynolds number whereas the peak total shear stress has a similar value in both cases. For both Reynolds num-

Table 2
Comparison of peak Reynolds stresses in natural and forced ($f_e/f_{v0} = 2.0$, $\Delta U/U_m = 0.10$) wakes

Study	*Re*	Mode	$\overline{u'u'}/U_m^2$	$\overline{v'v'}/U_m^2$	$\overline{u'v'}/U_m^2$	$\overline{\tilde{u}\tilde{u}}/U_m^2$	$\overline{\tilde{v}\tilde{v}}/U_m^2$	$\overline{\tilde{u}\tilde{v}}/U_m^2$
Kim et al. (2006)	360	Natural	0.18	0.38	0.09	0.14	0.34	0.08
		forced	0.30	0.52	0.12	0.24	0.47	0.12
Present results	2150	Natural	0.16	0.33	0.09	0.12	0.29	0.08
		forced	0.31	0.60	0.16	0.25	0.52	0.14

bers, the peak values are considerably magnified due to vortex shedding lock-on but the magnification appears more pronounced for the higher Reynolds number. However, turbulence effects mask the dynamics of vortex shedding. Therefore, it is more appropriate to compare directly the coherent contribution to the Reynolds stresses induced by vortex shedding. Table 2 shows that there is a close agreement in the peak values of the coherent Reynolds stresses for both natural and forced wakes at the two different Reynolds numbers compared. This result strongly supports the view that the effects of vortex shedding lock-on carry across a wide range of Reynolds numbers from few hundred up to several thousands so long as the attached boundary layer remains laminar until separation since the coherent contributions in the wakes of circular cylinders is similar over this range (Balachandar et al., 1997). However, it should be pointed out that the wake is more susceptible to vortex shedding lock-on at high Reynolds numbers since synchronization occurs over a wider range of frequencies for high Reynolds numbers as discussed in Konstantinidis et al. (2003). This might be attributed to differences in the details of boundary layer separation which poses an interesting issue for further study.

3.5. Vortex strength

The instantaneous velocity field in the cylinder wake exhibits both coherent and incoherent structures. The former are due to the organized flow induced by periodic vortex shedding from alternative sides of the cylinder while randomness ensues due to the turbulent nature of the wake at subcritical Reynolds numbers ($350 < Re < 2 \times 10^5$). As an example, Fig. 7 shows the distribution of out-of-plane vorticity ω_z computed from snapshots of the instantaneous velocity field in steady and forced flow. Velocity gradients were computed employing a least-squares formula (Raffel et al., 1998) in order to smooth distributions of the vorticity $\omega_z = \partial v/\partial x - \partial u/\partial y$. Vorticity values are normalized with the cylinder diameter and flow velocity, i.e. $\omega_z D/U$. Clearly, the distribution of instantaneous vorticity is associated with alternating vortex shedding from the sides of the cylinder in both cases. However, there are some notable differences between steady and forced flow; the shear layers are elongated and a region of irrotational (stagnant) fluid exists near the base of the cylinder for steady flow whereas the shear layers roll-up closer to the cylinder for forced flow, washing out the fluid from the base of the cylinder and the vortices are shed away from the centreline. In both cases, small-scale vortices are embedded on the shear layers separating from the sides of the cylinder, a typical feature for the Reynolds number investigated.

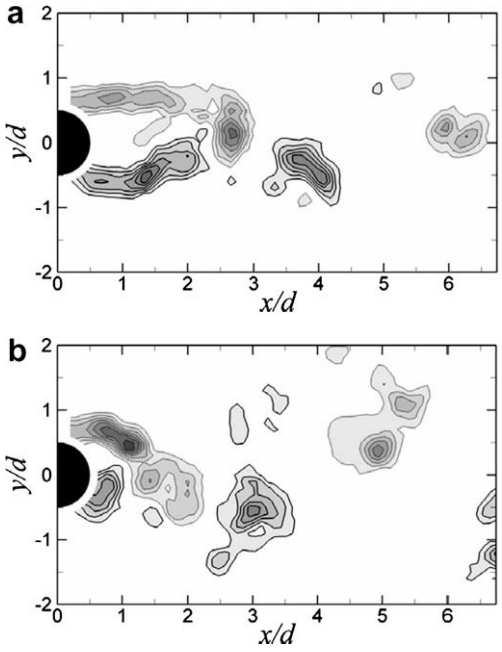

Fig. 7. Instantaneous snapshots of the out-of plane vorticity in the wake; (a) steady flow, (b) pulsating flow, $\Delta U/U_m = 0.23$. Contour levels: $\omega_z D/U = \pm 1, \pm 2, \ldots, \pm 8$.

The instantaneous vorticity distributions shown in Fig. 7 bear little information of the average strength of the vortices shed from the cylinder as the vorticity of the coherent structures is fragmented into pieces. In order to extract meaningful information from the instantaneous velocity fields, a conditional averaging methodology was employed. The methodology is based on the cross-correlation between velocity fields as a phase identifier and has been validated in Konstantinidis et al. (2005a). Selected results obtained from the above methodology are shown in Fig. 8 that shows phase-averaged vorticity distributions for three different amplitudes. Due to the averaging, the small-scale vortices embedded on the shear layers are filtered out. For steady flow (Fig. 8a), the shear layers emanating from the cylinder are elongated and roll-up further downstream at $x \approx 2\,d$. The superimposition of flow pulsations induces a shortening of the vortex formation region and the roll-up process takes place immediately behind the cylinder. This process causes the fluid to backwash the rear surface of the cylinder. With increasing forcing amplitude, the above effects become more pronounced until the vortex formation occurs in a very narrow region on the back of the cylinder (Fig 8c). These observations can explain the increased heat/mass transport rates from/to the cylinder back surface that have been observed in the lock-on range due to pulsating flow (Sung et al., 1994). It is also worth noting that Park and Gharib (2001) found that for a cylinder oscillating in cross-flow the increase in the heat transfer rate correlates inversely with the distance at which vortices roll-up behind the cylinder, i.e. when the heat transfer increases the distance decreases. The same scenario appears to be true for locked-on wakes in pulsating flow.

Fig. 9 shows the variation of the vortex strength with downstream distance from the cylinder for the different amplitudes employed. The strength Γ of the vortices shed from the cylinder was computed from the phase-averaged vorticity distributions using surface quadrature around the vortex cores as detailed in Konstantinidis et al. (2005b). The normalized vortex strength $\Gamma(x)/U_m d$ initially increases, reaches a maximum value and then decreases with the distance from the cylinder. It is worth noting that extrapolation of the present data to a distance $x = 7\,d$ compares favourably with the strength estimates of Armstrong et al. (1987) for both steady and pulsating flow. The location of maximum strength shifts closer to the cylinder with increasing amplitude ratio. Within the uncer-

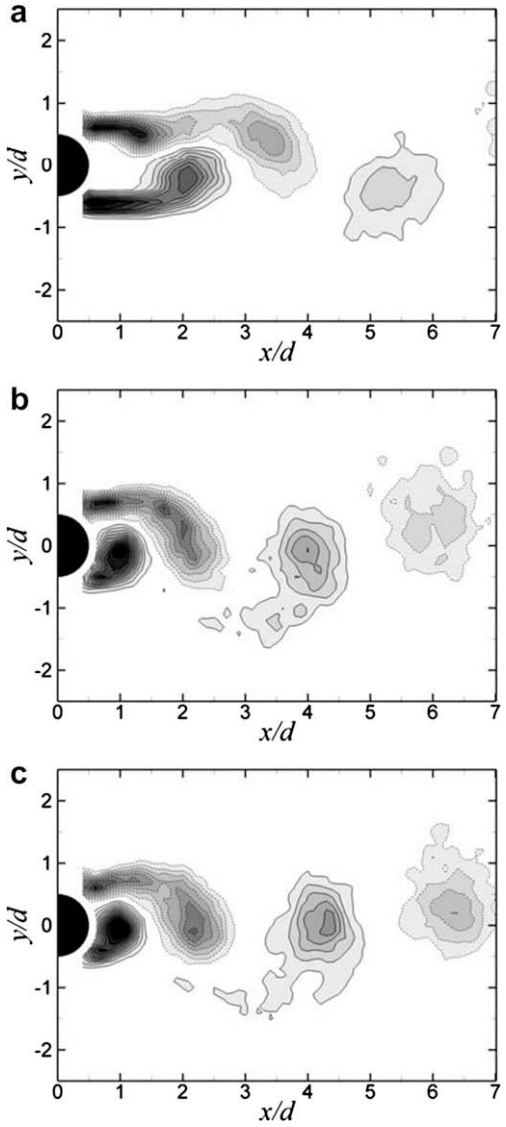

Fig. 8. Distributions of phase-averaged vorticity for different amplitude ratios; (a) $\Delta U/U_m = 0.00$, (b) 0.12, (c) 0.23. Contour levels: $\omega_z D/U = \pm 0.5, \pm 1, \ldots, \pm 5$.

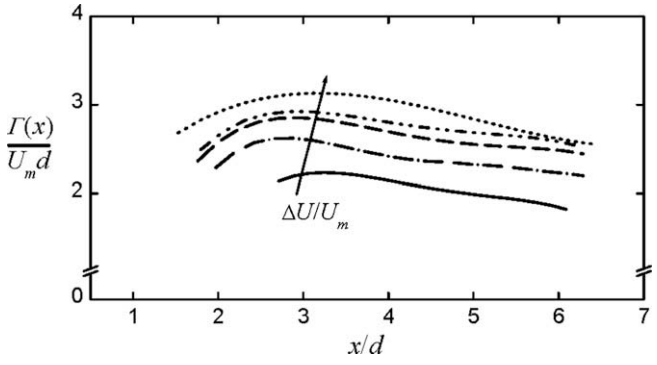

Fig. 9. Variation of normalized vortex strength with longitudinal distance from the cylinder for different amplitude ratios.

tainty of the data, the maximum value Γ_{max} increases almost linearly with the amplitude as shown in Fig. 10. However, a careful examination of the data might indicate that the rate of increase is slightly higher at low amplitudes than at the two highest amplitudes employed. This observation agrees with the variation of the maxima in the Reynolds stresses with amplitude in Figs. 3 and 4. As discussed earlier, it might be expected that the strength of the coherent vortices cannot increase indefinitely with amplitude but there is no data available at higher amplitudes to pursue this argument further.

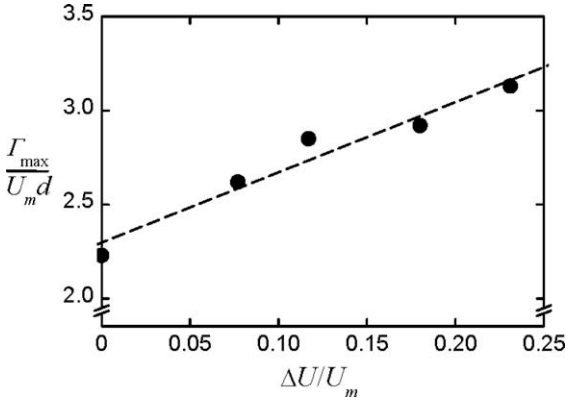

Fig. 10. Variation of peak vortex strength with amplitude ratio.

3.6. Drag force coefficient

The mean drag force on the cylinder can be estimated from wake measurements using a momentum-based approach (Antonia and Rajagopalan, 1990). The drag coefficient is given by

$$C_D = 2\int_{-\infty}^{\infty} \frac{\bar{U}}{U_e}\left(\frac{U_e-\bar{U}}{U_e}\right)\mathrm{d}\left(\frac{y}{d}\right) + 2\int_{-\infty}^{\infty}\left(\frac{\overline{v^2}-\overline{u^2}}{U_e^2}\right)\mathrm{d}\left(\frac{y}{d}\right) \quad (7)$$

where U_e is the velocity of the 'undisturbed' flow outside the wake. The drag coefficient was estimated from wake measurements at different stations downstream from the cylinder. For short distances from the cylinder, i.e. less than the recirculation bubble length where strong overshoots in the mean velocity profiles exist, Eq. (7) resulted in rapidly increasing values of the drag coefficient which were unacceptably low. Further downstream in the region $3 < x/d < 7$, U_e varied by less than 1% and the estimates of the drag coefficient exhibited only small deviations from a constant value. The drag coefficient for steady flow ($C_D = 1.19$) estimated from Eq. (7) agrees well with reported values in the published literature considering the flow blockage (10%) in the present study. For example, the drag coefficient may be compensated for the proximity of solid walls as suggested by Allen and Vincenti (see Roshko, 1961)

$$\frac{C_D'}{C_D} = 1 - \frac{1}{2}C_D\left(\frac{d}{h}\right) - 2.5\left(\frac{d}{h}\right)^2 \quad (8)$$

where C_D is the measured and C_D' is the corrected value of the drag coefficient, h is the width of the flow domain and d/h is the blockage ratio. Implementing the above correction yields a drag coefficient value equal to 1.09, i.e. 8% lower than the value determined directly from Eq. (7).

Fig. 11 shows the variation of the mean drag coefficient with amplitude ratio (not corrected for blockage). Error bars indicate the standard deviation between the estimates at different longitudinal stations. Within the uncertainty of the data, the results indicate that there is a linear increase of the drag coefficient with amplitude ratio. The results from the present study are compared with those from other experimental studies in Fig. 12. Armstrong et al. (1986) and Jarza and Podolski (2004) employed surface pressure measurements on a cylinder in pulsating air flows. Nishihara

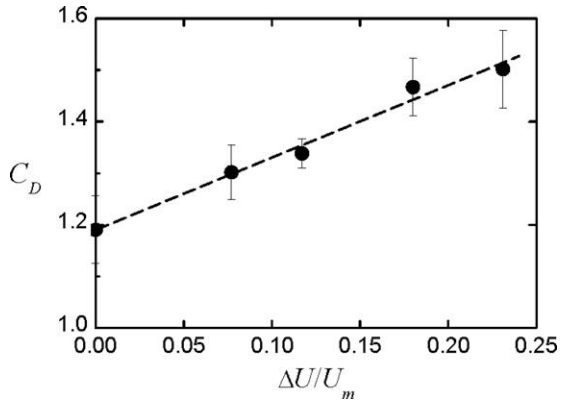

Fig. 11. Variation of drag force coefficient with amplitude ratio.

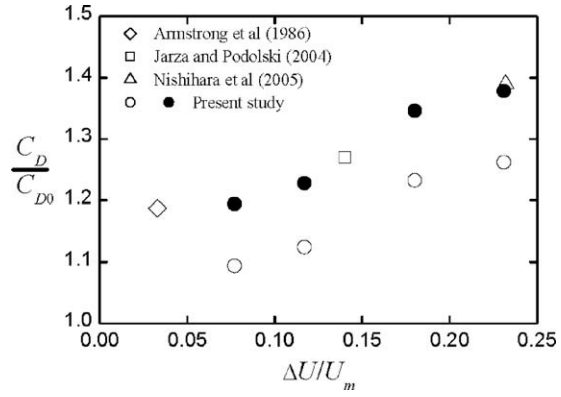

Fig. 12. Variation of the normalized drag coefficient with amplitude ratio.

et al. (2005) studied the analogous case of a cylinder oscillating along the flow direction and employed direct measurements of the forces with strain gauges in water. In order to compare the results from the latter study to the present one, the amplitude of cylinder oscillation (X_o) is converted into an equivalent amplitude of velocity oscillation, $\Delta U = 2\pi f_e X_o$, or $\Delta U/U_m = 2\pi(X_o/d)(f_e/f_0)St$ in dimensionless form. The drag coefficient normalized with its value in the unforced wake (C_{D0}), is approximately 8% lower in the present study than that in the other studies (open circles in Fig. 12). This deviation might be attributed to differences in the experimental configurations (particularly blockage), measurement techniques and Reynolds numbers employed. However, if C_{D0} is corrected for blockage using Eq. (8) then the corrected data (full circles in Fig. 12) overlap with the other published data. The present results indicate that the drag force variation correlates well with the inverse of the recirculation bubble length and the vortex formation length (shown earlier). This is consistent with the findings of Park and Gharib (2001) on heat transfer enhancement based on the Reynolds analogy between momentum and heat transport.

4. Conclusions

The present study showed that the wake structure of a circular cylinder is amenable to systematic modifications by flow pulsations when the lock-on phenomenon takes place, i.e. when the forcing frequency is around twice that of vortex shedding without forcing. The effect of increasing pulsation amplitude is to reduce the extent of the recirculation bubble and vortex formation region, increase the magnitude of the velocity fluctuations and the corresponding Reynolds stresses in the wake. These modifications are caused primarily by changes in the vortex dynamics in the formation region. The shear layers separating from the cylinder sides roll-up closer to the cylinder with increasing amplitude inducing a strong transverse oscillation of the wake. As a result, vortex strength and the drag force coefficient scale almost linearly with forcing amplitude. Similar amplitude effects were observed at different forcing frequencies within the lock-on range but these were less marked away from resonant forcing. Comparisons with the published literature indicate that the effects of vortex shedding lock-on carry across a wide range of Reynolds numbers and, to some extend, to different methods inducing lock-on; hence, it might be possible to extrapolate data from different configurations at least for relatively small perturbation amplitudes. The above results can explain associated changes in heat/mass transfer found in related studies.

Acknowledgments

The help from Dr. David Hann in setting up the experiments and the financial support from the EPSRC through Grant GR/R29802/01 are gratefully acknowledged.

References

Al-Asmi, K., Castro, I.P., 1992. Vortex shedding in oscillatory flow: geometrical effects. Flow Measurement and Instrumentation 3, 187–202.
Antonia, R.A., Rajagopalan, S., 1990. Determination of drag of a circular cylinder. AIAA Journal 28, 1833–1834.
Armstrong, B.J., Barnes, F.H., Grant, I., 1986. The effect of a perturbation on the flow over a bluff cylinder. Physics of Fluids 29, 2095–2102.
Armstrong, B.J., Barnes, F.H., Grant, I., 1987. A comparison of the structure of the wake behind a circular cylinder in steady flow with that in a perturbed flow. Physics of Fluids 30, 19–26.
Balachandar, S., Mittal, R., Najjar, F.M., 1997. Properties of the mean recirculation region in the wakes of two-dimensional bluff bodies. Journal of Fluid Mechanics 351, 167–199.
Barbi, C., Favier, D.P., Maresca, C.A., Telionis, D.P., 1986. Vortex shedding and lock-on of a circular cylinder in oscillatory flow. Journal of Fluid Mechanics 170, 527–544.
Barnes, F.H., Grant, I., 1983. Vortex shedding in unsteady flow. Journal of Wind Engineering and Industrial Aerodynamics 11, 335–344.
Breuer, M., 2000. A challenging test case for large eddy simulation: high Reynolds number circular cylinder flow. International Journal of Heat and Fluid Flow 21 (5), 648–654.
Choi, H., Jeon, W.P., Kim, J., 2008. Control of flow over a bluff body. Annual Review of Fluid Mechanics 40, 113–139.
Graftieaux, L., Michard, M., Grosjean, N., 2001. Combining PIV, POD and vortex identification algorithms for the study of unsteady turbulent swirling flows. Measurement Science and Technology 12, 1422–1429.
Griffin, O.M., 1978. A universal Strouhal number for the 'locking-on' of vortex shedding to the vibrations of bluff cylinders. Journal of Fluid Mechanics 85, 591–606.
Griffin, O.M., 1995. A note on bluff body vortex formation. Journal of Fluid Mechanics 284, 217–224.
Griffin, O.M., Hall, H.S., 1991. Vortex shedding lock-on and flow control in bluff body wakes – review. ASME Journal of Fluids Engineering 113, 283–291.
Jarza, A., Podolski, M., 2004. Turbulence structure in the vortex formation region behind a circular cylinder in lock-on conditions. European Journal of Mechanics – B/Fluids 23 (3), 535–550.
Keane, R.D., Adrian, R.J., 1990. Optimization of particle image velocimeters. Part I: double pulsed systems. Measurement Science and Technology 1, 1202–1215.
Kikuchi, Y., Suzuki, H., Kitagawa, M., Ikeya, K., 2000. Effect of pulsating Strouhal number on heat transfer around a heated cylinder in pulsating cross-flow. JSME International Journal 43, 250–257.
Kim, W., Yoo, J.Y., Sung, J., 2006. Dynamics of vortex lock-on in a perturbed cylinder wake. Physics of Fluids 18, 074103.
Konstantinidis, E., Balabani, S., Yianneskis, M., 2003. The effect of flow perturbations on the near wake characteristics of a circular cylinder. Journal of Fluids and Structures 18, 367–386.
Konstantinidis, E., Balabani, S., Yianneskis, M., 2005a. Conditional averaging of PIV plane wake data using a cross-correlation approach. Experiments in Fluids 39, 38–47.
Konstantinidis, E., Balabani, S., Yianneskis, M., 2005b. The timing of vortex shedding in a cylinder wake imposed by periodic inflow perturbations. Journal of Fluid Mechanics 534, 45–55.
Konstantinidis, E., Balabani, S., Yianneskis, M., 2007. Bimodal vortex shedding in a perturbed cylinder wake. Physics of Fluids 19, 011701.

Ma, X., Karniadakis, G.E., Park, H., Gharib, M., 2003. DPIV-driven flow simulation: a new computational paradigm. Proceedings of the Royal Society of London Series a-Mathematical Physical and Engineering Sciences 459, 547–565.

Mittal, S., 2001. Computation of three-dimensional flows past circular cylinder of low aspect ratio. Physics of Fluids 13 (1), 177–191.

Nishihara, T., Kaneko, S., Watanabe, T., 2005. Characteristics of fluid dynamic forces acting on a circular cylinder oscillated in the streamwise direction and its wake patterns. Journal of Fluids and Structures 20, 505–518.

Park, H.G., Gharib, M., 2001. Experimental study of heat convection from stationary and oscillating circular cylinder in cross flow. Journal of Heat Transfer 123 (1), 51–62.

Patte-Rouland, B., Lalizel, G., Moreau, J., Rouland, E., 2001. Flow analysis of an annular jet by particle image velocimetry and proper orthogonal decomposition. Measurement Science and Technology 12, 1404–1412.

Perwaiz, J., Base, T.E., 1992. Heat-transfer from a cylinder and finned tube in a pulsating cross-flow. Experimental Thermal and Fluid Science 5 (4), 506–512.

Raffel, M., Willert, C., Kompenhans, J., 1998. Particle Image Velocimetry: A Practical Guide. Springer.

Roshko, A., 1961. Experiments on the flow past a circular cylinder at very high Reynolds number. Journal of Fluid Mechanics 10, 345–356.

Sung, H.J., Hwang, K.S., Hyun, J.M., 1994. Experimental study on mass-transfer from a circular-cylinder in pulsating flow. International Journal of Heat and Mass Transfer 37 (15), 2203–2210.

Telionis, D.P., Gundappa, M., Diller, T.E., 1992. On the organization of flow and heat-transfer in the near wake of a circular-cylinder in steady and pulsed flow. ASME Journal of Fluids Engineering 114 (3), 348–355.

Wolochuk, M.C., Plesniak, M.W., Braun, J.E., 1996. The effects of turbulence and unsteadiness on vortex shedding from sharp-edged bluff bodies. ASME Journal of Fluids Engineering 118, 18–25.